Annals of Biomedical Engineering
https://doi.org/10.1007/s10439-023-03346-3

ORIGINAL ARTICLE

Modeling Ventilator-Induced Lung Injury and Neutrophil Infiltration to Infer Injury Interdependence

Courtney L. Mattson[1] · **Bradford J. Smith**[1,2]

Received: 13 March 2023 / Accepted: 7 August 2023

Abstract

Acute respiratory distress syndrome (ARDS) and ventilator-induced lung injury (VILI) are heterogeneous conditions. The spatiotemporal evolution of these heterogeneities is complex, and it is difficult to elucidate the mechanisms driving its progression. Through previous quantitative analyses, we explored the distributions of cellular injury and neutrophil infiltration in experimental VILI and discovered that VILI progression is characterized by both the formation of new injury in quasi-random locations and the expansion of existing injury clusters. Distributions of neutrophil infiltration do not correlate with cell injury progression and suggest a systemic response. To further examine the dynamics of VILI, we have developed a novel computational model that simulates damage (cellular injury progression and neutrophil infiltration) using a stochastic approach. Optimization of the model parameters to fit experimental data reveals that the range and strength of interdependence between existing and new damaged regions both increase as mechanical ventilation patterns become more injurious. The interdependence of cellular injury can be attributed to mechanical tethering forces, while the interdependence of neutrophils is likely due to longer-range cell signaling pathways.

Keywords Mechanical ventilation · Cellular automata · Stochastic model · Numerical optimization · Mouse model · Spatiotemporal heterogeneity

Introduction

Critical illness, such as COVID-19, and severe injury may cause acute respiratory distress syndrome (ARDS). ARDS is a dangerous and potentially fatal respiratory condition with approximately a 40% mortality rate [1]. Positive pressure ventilation is key to the management of ARDS because it can allow patients to maintain gas exchange [2]. Despite its life saving necessity, mechanical ventilation can lead to ventilator-induced lung injury (VILI), which exacerbates the deficits of the injured lung through overdistension (volutrauma), cyclic collapse and reopening of the distal airspaces (atelectrauma), and inflammatory responses (biotrauma) [3–9].

Spatiotemporal heterogeneity is a characteristic of both ARDS and VILI. The distribution of ventilation is inherently heterogeneous due to the effects of gravity, lung anatomy, and localized injury. This results in variability in alveolar tidal volumes, septal strains, and extent of participation in gas exchange throughout the lung. Ventilation distribution is also dependent on the applied pressures [10] and ventilation patterns [11], and the degree of alveolar ventilation heterogeneity has been shown to increase with injury [12–14]. In severe cases of ARDS and VILI, collapse or flooding of the alveoli and small airways results in a substantial reduction in the fraction of the lung available to accept incoming gas; this phenomenon is referred to as 'baby lung' [15]. These alterations in regional mechanics also occur at smaller length scales where the flooding of alveoli increases distension in adjacent patent regions [16] due to the physical interconnections between the alveoli (parenchymal tethering). The field-to-field variability of this heterogeneity has been quantified using markers such as edema, cellular damage, and alveolar collapse [17–22]. Organ-scale-imaging

Associate Editor Merryn Tawhai oversaw the review of this article.

✉ Bradford J. Smith
Bradford.Smith@cuanschutz.edu

[1] Department of Bioengineering, University of Colorado Denver | Anschutz Medical Campus, 12705 E. Montview Blvd., Suite 100, Aurora, CO 80045, USA

[2] Pulmonary and Sleep Medicine, Department of Pediatrics, School of Medicine, University of Colorado, Aurora, CO, USA

techniques have also shown the heterogeneous regional distributions of injury and inflammation [23–26], despite at a lower spatial resolution than can be achieved with light microscopy.

However, the dynamic changes in heterogeneities during injury progression are complex, and the underlying mechanisms driving the progression are difficult to elucidate. One approach to understanding the causes and effects of spatial heterogeneity is through computational approaches such as the finite element method (FEM) that allow analysis of the microscale pattern of stress and strain propagation based on parenchymal tethering forces [27–30]. However, validation and verification of these predictions through experiments remains an elusive goal.

Our recent experimental study [31] analyzed both the micro- and macro-scale distributions of cellular injury as VILI progressed and revealed that new injury forms in quasi-random locations and also propagates outward from sites of existing injury. Leukocyte recruitment also occurs during VILI [3, 4, 32–34], but the pattern of infiltration suggests a systemic response [31]. To better explain the spatiotemporal evolution of injury, the current study uses a novel computational model, fit to experimental data, to recapitulate our *in vivo* quantification of injury propagation during VILI. This inverse modeling approach facilitates more thorough analysis of the complex experimental results.

In this custom computational model, a synthesized grid of initially healthy cells undergoes various simulated ventilation patterns which causes injury development and neutrophil recruitment. Optimization of the model parameters to fit our experimental data [31] reveals the range and strength of interdependence between existing and new damage. The parameters governing this interdependence allow us to understand how damage is occurring and how its progression changes under different ventilation conditions. Model optimizations reveal significant parameter differences between cell injury formation and neutrophil infiltration, suggesting different driving mechanisms for each process.

Materials and Methods

A glossary of symbols and abbreviations is provided in Table 1.

Previous Experimental Data

Previous Animal Experiments

In previously published work, we ventilated initially healthy mice with three ventilation protocols: *Protect* ventilation (positive end-expiratory pressure (PEEP) = 3 cmH_2O, respiratory rate (RR) = 250 breaths/min, and set tidal volume (V_T) = 7 mL/kg); *p30* ventilation (PEEP = 0 cmH_2O, RR = 50 breaths/min, and plateau pressure (Pplat) = 30 cmH_2O); or *p37.5* ventilation (PEEP = 0 cmH_2O, RR = 50 breaths/min, and Pplat = 37.5 cmH_2O). Elastance measurements were taken throughout ventilation to track the inflicted changes in respiratory mechanics. Tissue was harvested after elastance had minimally increased, doubled, and quadrupled for the injuriously ventilated groups (*p30* and *p37.5*). *Protect* ventilation was terminated after ~ 4.5 hours to match the longest ventilation time of the injurious ventilation groups. The changes in elastance as ventilation progresses are shown in Fig. 1A. An additional *Control* group received only 10 minutes of stabilizing ventilation before the tissue was harvested. Each group consists of 5 subjects. Independent uniform random sections of tissue are stained, imaged, and analyzed to identify the locations of all cell nuclei (DAPI +), injured cells (PI + , Fig. 1B–E, red dots), and neutrophils (Ly6G +). The area occupied by lung tissue was also segmented (Fig. 1B, white) using the signal from the DAPI channel [31].

Overall Density

The overall density, in cells per area, of each marked cell type (DAPI + , PI + , Ly6G +) is calculated for each section of tissue (e.g. Fig. 1B–E, # red PI + points per white area in μm^2). These densities are normalized by total lung volume [31]. The mean and standard deviation of overall density are then calculated for the control and experimental groups using each section of tissue (~20 sections per mouse, ~ 100 sections per group) as a data point.

Density-Based Spatial Clustering of Applications with Noise (DBSCAN)

Tightly packed regions of PI + and Ly6G + cells were identified using the Density-Based Spatial Clustering of Applications with Noise algorithm (DBSCAN) [31]. In the current study, we use the portion of that analysis that groups together cells within 30 µm of each other. Figure 2 shows the DBSCAN clustering for representative sections with moderate (Fig. 2A, 2*xH30* section) and severe (Fig. 2B, 4*xH30* section) injury. The per-animal mean and standard deviation of the number of cells (either PI + or Ly6G +) in each cluster are used as an input data point for the model fitting.

Computational Model of Injury Progression

A probabilistic cellular automata model is developed to recapitulate and analyze the spatiotemporal evolution of damage (cellular injury and neutrophil accumulation) observed in the experimental data. A synthesized grid of initially healthy lung cells (Fig. 3A, white dots) undergoes simulated ventilation; the likelihood of any individual 'cell' becoming damaged is a

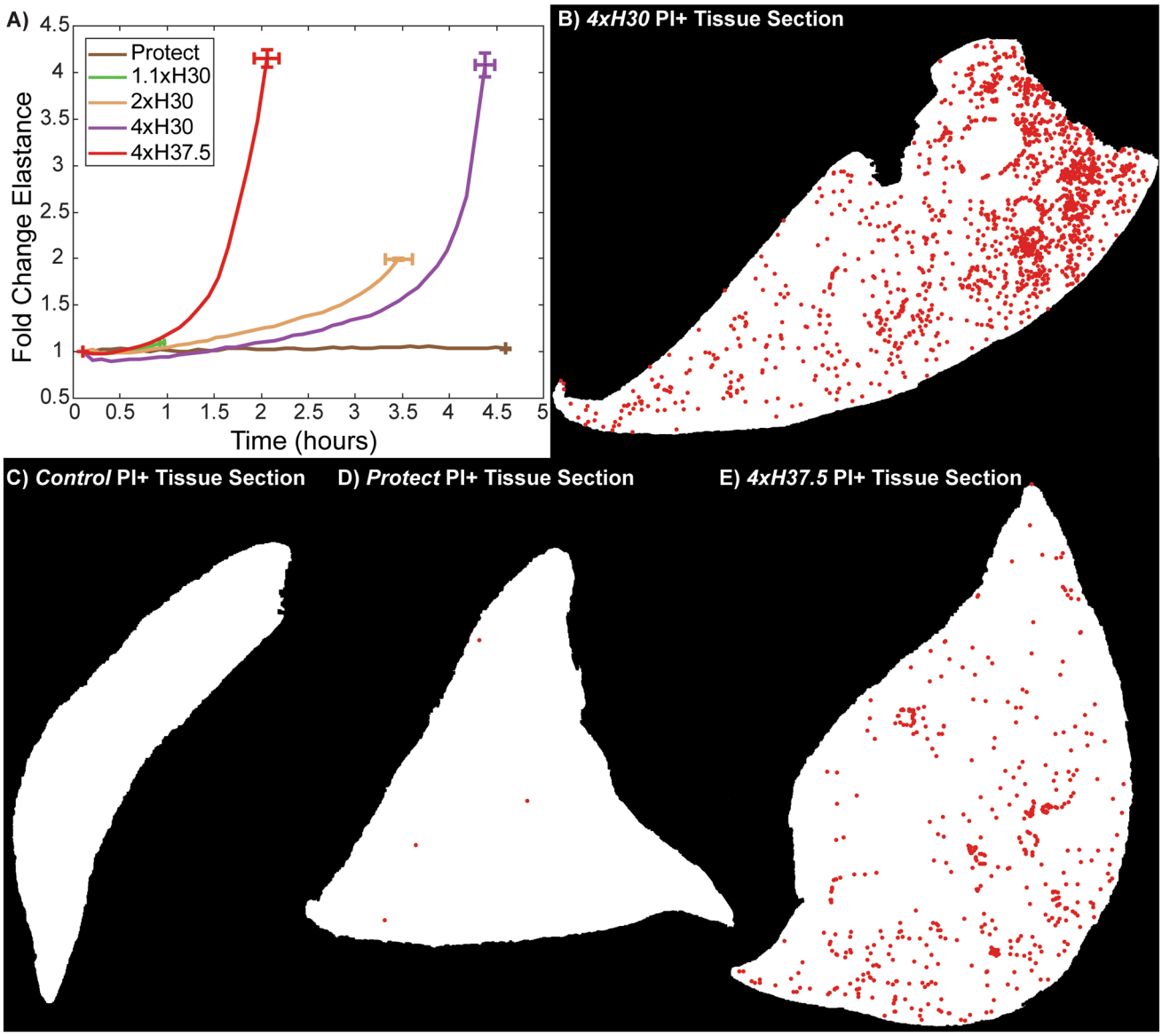

Fig. 1 **A** Fold changes in respiratory elastance (H) as a function of ventilation time. Ventilation is terminated based on the desired level of inflicted injury as measured by fold change in H for all injuriously ventilated groups: *1.1xH30*, *2xH30*, *4xH30*, and *4xH37.5*. *Protect* ventilation is stopped after a set time of ~4.5 h. **B–E** Identification of lung tissue (white area) and centroids of injured cells (red dots) in a fluorescent microscopy image of a whole lung lobe. These data come from our prior experiments [31]. **B** Representative lung section from *p30* group. **C** Representative lung section from *Control* group. **D** Representative lung section from *Protect* group. **E** Representative lung section from *p37.5* group

combination of a baseline level of probability and a probability increase based on the local concentration of damaged cells. At any given timestep, the likelihood of each 'cell' becoming damaged is defined by

$$P_{Inj} = P_{Base} + \left(\frac{\#_{Inj}(r)}{\#_{Tot}(r)} \times P_{Local} \right), \quad (1)$$

where P_{Inj} represents the probability of any given 'cell' becoming damaged and P_{Base} represents the baseline probability of damage occurring in a cell that is currently undamaged. To account for damage interdependence, $\#_{Inj}$ represents the number of existing damaged 'cells' (Fig. 3B, red dots) within the region of influence (Fig. 3B, blue shaded) which is defined by radius, r (Fig. 3B, black arrow), $\#_{Tot}$ represents the total number of 'cells' within that region of influence, and P_{Local} represents the coefficient of probability increase based on the local concentration of damaged cells. For each point at every timestep, P_{Inj} is compared to a random number drawn from a uniform distribution

Table 1 Glossary of symbols and abbreviations

Symbol or abbreviation	Definition
Control	Experimental group minimally ventilated
Protect	Experimental group ventilated with PEEP = 3 cmH_2O, RR = 250 breaths/min, and set V_T = 7 mL/kg for ~ 4.5 hours
p30	Experimental groups ventilated with PEEP = 0 cmH_2O, RR = 50 breaths/min, and Pplat = 30 cmH_2O
1.1xH30	Experimental group ventilated with *p30* ventilation until a minimal (1.1x) increase in elastance (H)
2xH30	Experimental group ventilated with *p30* ventilation until a doubling (2x) increase in elastance (H)
4xH30	Experimental group ventilated with *p30* ventilation until a quadrupling (4x) increase in elastance (H)
p37.5	Experimental groups ventilated with PEEP = 0 cmH_2O, RR = 50 breaths/min, and Pplat = 37.5 cmH_2O
4xH37.5	Experimental group ventilated with *p37.5* ventilation until a quadrupling (4x) increase in elastance (H)
P_{Inj}	Probability of any given simulated cell becoming damaged
P_{Base}	Baseline probability of damage occurring in a simulated cell that is currently undamaged
P_{Local}	Coefficient of probability increase based on the local concentration of damaged cells
r	Radius defining the region of influence
$\#_{Inj}$	Number of existing damaged simulated cells within the region of influence
$\#_{Tot}$	Total number of simulated cells within that region of influence
t_{step}	Timestep
$P_{Base\ Pre-Normalization}$	P_{Base} prior to being normalized by the timestep size
$P_{Local\ Pre-Normalization}$	P_{Local} prior to being normalized by the timestep size
O_F	Objective function
N	Number of time points analyzed for any given experimental group
μ_D^E	Mean of overall density of experimental data
μ_D^S	Mean of overall density of simulated data
σ_D^E	Standard deviation of overall density of experimental data
σ_D^S	Standard deviation of overall density of simulated data
μ_C^E	Mean of cluster size of experimental data
μ_C^S	Mean of cluster size of simulated data
σ_C^E	Standard deviation of cluster size of experimental data
σ_C^S	Standard deviation of cluster size of simulated data

(MATLAB *rand*) between 0 and 1. An undamaged cell becomes damaged if $P_{Inj} > rand$, and it is currently undamaged. The random number generator is seeded with a unique number based on the current date and time (MATLAB *now* function).

To mimic the *in vivo* conditions and experimental data sampling, the damage progresses on a 3-dimensional grid and 2-dimensional planes of that grid are sampled for analysis. Figure 3C demonstrates how simulated damage progresses in the 3-dimensional cube. The model parameters are algorithmically optimized to match the mean and standard deviation of both tissue density and DBSCAN cluster sizes, as described in the above sections, *Overall Density* and *DBSCAN*.

Defining Model Parameters

The model outcome is affected by the setting of static parameters: total cell density, sampling spacing, grid size (length of cubic synthesized grid of 'cells'), timestep, and number of iterations (repeated runs for each unique set of parameters). The initial cubic grid is composed of uniformly distributed cells (potential sites of damage) with density equal to that of all cells in the experimental lung sections (total cell density = 3.7×10^{-3} cells/μm^2). Every x–y plane is sampled and

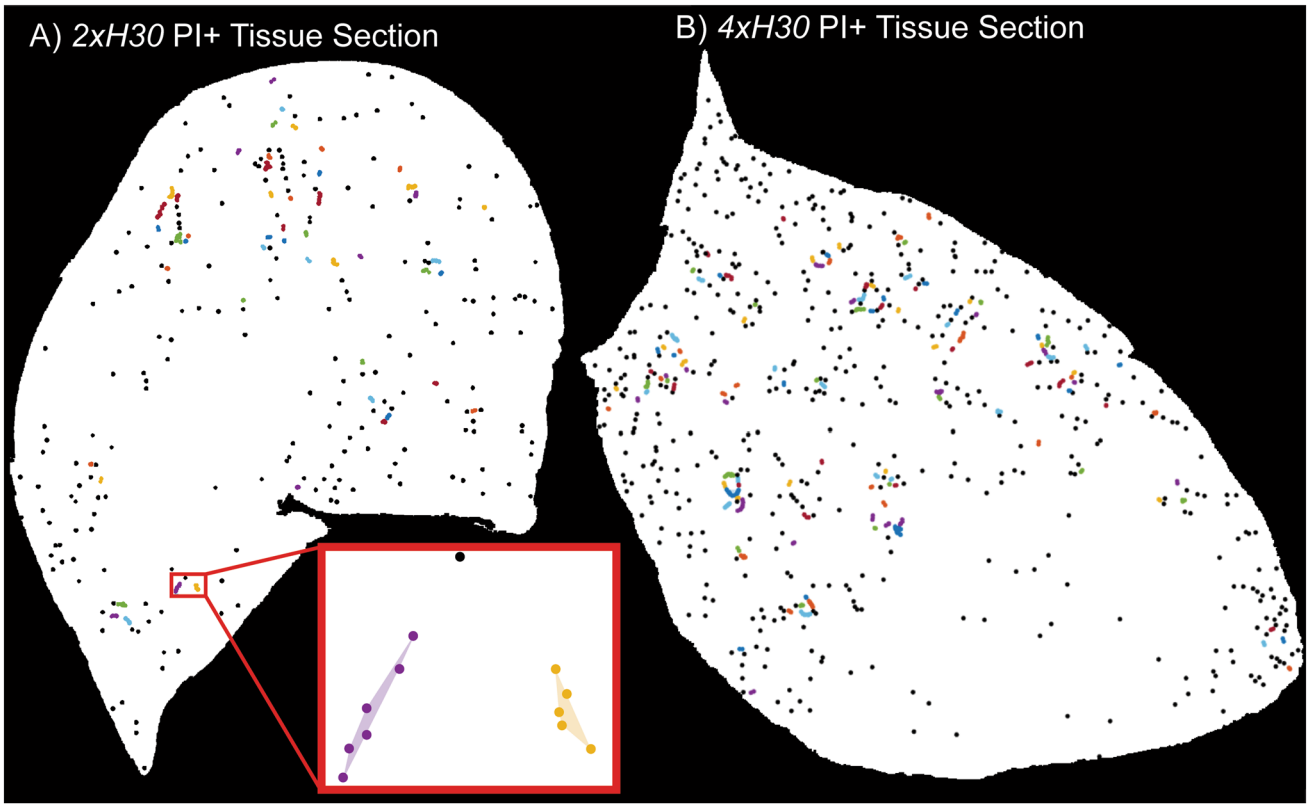

Fig. 2 Density-Based Spatial Clustering of Applications with Noise (DBSCAN) groups identified cells into clusters (*inset* in *A*, purple dots with shaded area and yellow dots with shaded area) while allowing isolated cells to remain unclustered (*inset* in *A*, black dot). These data come from our prior experiments [31]. Each group of colored dots represents a distinct cluster of cellular injury. The identified neutrophils are not shown in these figures. **A** Representative section from *2xH30* showing moderate cellular injury (PI+). **B** Representative section from 4*xH30* showing severe cellular injury (PI+)

used as a 'tissue section' for analysis (sampling spacing = 1 cell). Simulated tissue sections are analyzed identically to the experimental tissue sections. We sample every plane to maximize the output data from each simulation.

Settings for grid size, timestep, and number of iterations are selected to provide the most computationally efficient model that still yields stable results (Fig. 4A–D) using the *p37.5* ventilation cellular injury data. This group requires the most computationally expensive set of static parameters because it has the shortest ventilation time and most rapid injury progression (requiring the smallest time step to stabilize) and has the most heterogeneous distribution of injury (homogenous distributions stabilize at a smaller grid size and larger time step than heterogeneous distributions). The best-fit variable parameters for the *p37.5* ventilation cellular injury group are analyzed at a variety of grid size, timestep, and iteration values. The combination of these static parameters that minimizes run time and maximizes model precision is found through a combination of automated and manual iterating with various combinations.

All experimental groups for both cellular injury progression and neutrophil infiltration use the same static parameter values (total cell density, sampling spacing, grid size, timestep, and number of iterations).

Optimized Parameters

P_{Base} (baseline probability of damage occurring), P_{Local} (strength of interdependence between damaged regions), and r (range of interdependence between damaged regions) are algorithmically optimized to fit the model to our experimental data. P_{Base} and P_{Local} are continuous variables. Because the grid is made of uniform distributed points, r is a discrete variable. Both P_{Base} and P_{Local} values are affected by changes in the timestep size. Accordingly, the following equations are used to eliminate the timestep size-dependence of those probabilities:

$$P_{Base} = P_{Base\,Pre-Normalization} \times t_{step}, \tag{2}$$

$$P_{Local} = P_{Local\,Pre-Normalization} \times t_{step}^{1.7}. \tag{3}$$

These equations are developed by analyzing the relationship between the model output and timestep when P_{Base} or

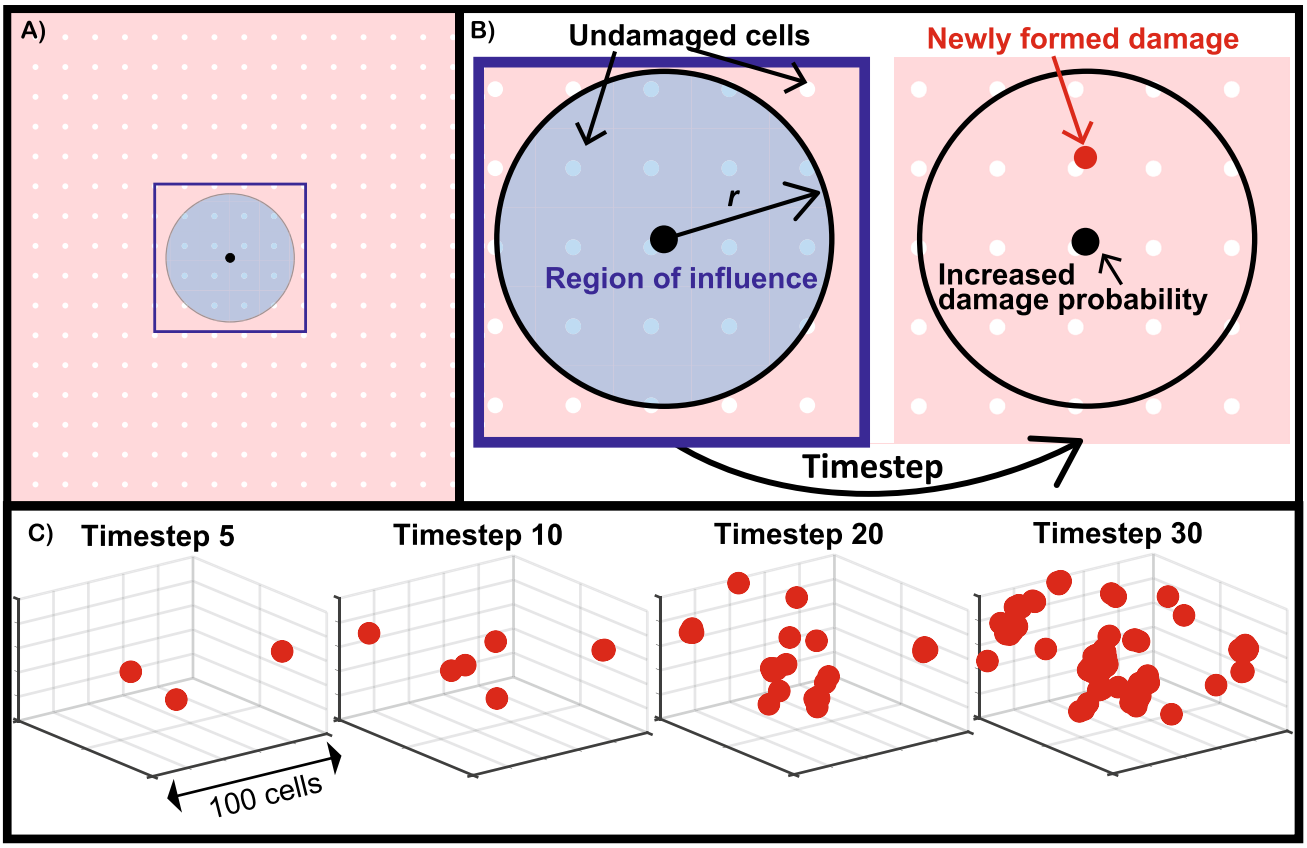

Fig. 3 **A** Grid of initially healthy simulated 'cells' (white dots). **B** Schematic of increased damage probability due to local concentration of damage. The likelihood of the central cell (black dot) becoming damaged increases as damage (red dot) forms within the region of influence (blue shaded circle), defined by radius of interdependence, *r* (black arrow). The diagram is shown in 2-dimensions for ease of understanding; the simulations are conducted in 3-dimensions. **C** Demonstration of damage progression in 3-dimensions. Damaged cells (red dots) develop in clusters as simulated ventilation progresses

P_{Local} are held constant. The relationship between P_{Base} and timestep is linear (Equation 2); the relationship between P_{Local} and timestep is exponential where a linear fit of the log–log relationship has a slope of 1.7 (Equation 3). These relationships are graphically shown in Supplemental Fig. S1 A&B.

Using these equations makes a more robust timestep-independent model. They also allow for faster preliminary computations, with larger time steps, to determine the constraints for each optimized parameter.

Modeling Injury Progression vs. Neutrophil Infiltration

For the simulated PI + (cellular injury) progression, the initial grid is made up of entirely healthy cells because the *Control* tissue had essentially no PI + cells. The objective function for parameter optimization in the cell injury simulations consists of the mean and standard deviation of overall PI + density as well as the mean and standard deviation of DBSCAN PI + cluster size. The DBSCAN analysis for the simulated injury groups adjacent cells into clusters ($d = 1$ cell *or* 33 μm); this is the smallest Euclidean distance that can be used on the synthesized uniform grid of cells. This is similar to the distance used for the experimental data ($d = 30$ μm). All other parameters are identical to the *cellular spacing DBSCAN* used for the experimental data [31].

The injury progression is simulated for *p30*, *p37.5*, and *Protect* groups to match the experimental ventilation durations. *p30* data were collected after 0.94 hours of simulated ventilation (*1.1xH30* experimental group—minimal increase in elastance), 3.46 hours of simulated ventilation (*2xH30* experimental group—doubling of elastance), and 4.38 hours of simulated ventilation (*4xH30* experimental group—quadrupling of elastance). *p37.5* data were collected after 2.06 hours of simulated ventilation (*4xH37.5* experimental group—quadrupling of elastance). *Protect* ventilation was simulated for 4.58 hours (*Protect* experimental group—duration chosen to match the longest ventilation time of the injuriously ventilated animals).

The objective function for cellular injury progression is

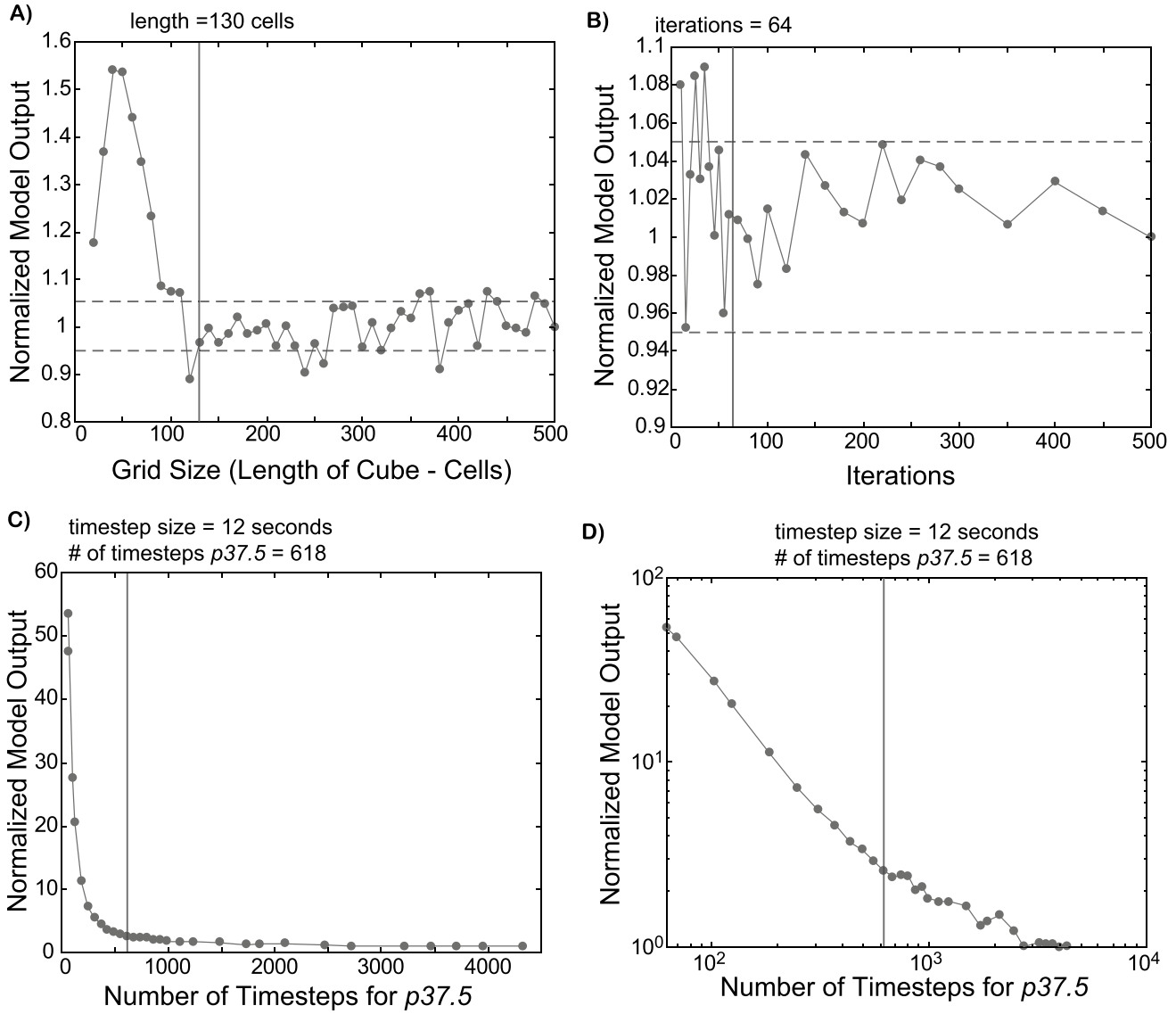

Fig. 4 Normalized model output refers to the objective function normalized by the output for the last (most computationally expensive) value. All analyses are performed on the *p37.5* ventilation cellular injury data. **A** Normalized model output versus grid size (edge length of cubic synthesized grid of 'cells'). The smallest grid size that provides results within 5% (dotted lines) of the last sampled value is chosen for the model optimization. A grid length of 130 cells is used for model optimization (gray line). **B** Normalized model output versus the number of iterations run for each unique set of parameters. The optimized model is run for 64 iterations at each set of parameters (gray line). **C** Normalized model output versus number of simulation timesteps for the *p37.5* group. A timestep of 12 seconds (618 total timesteps for *p37.5* group) is selected for model optimizations (gray line). **D** Log–log plot of normalized model output versus number of timesteps for *p37.5* group

$$O_F = \frac{1}{N}\sum_{i=1}^{N}\left(\left|\frac{\left(\mu_D^E-\mu_D^S\right)}{\mu_D^E}\right|+\left|\frac{\left(\sigma_D^E-\sigma_D^S\right)}{\sigma_D^E}\right| +\left|\frac{\left(\mu_C^E-\mu_C^S\right)}{\mu_C^E}\right|+\left|\frac{\left(\sigma_C^E-\sigma_C^S\right)}{\sigma_C^E}\right|\right), \tag{4}$$

where O_F is the objective function, N is the number of timepoints analyzed in the experimental group, μ is the mean, σ is the standard deviation, subscript D is overall density, subscript C is the cluster size, superscript E is experimental data, and superscript S is simulated data. The difference between each component of the objective function is divided by the experimental value to ensure that each component is weighted evenly.

For simulated neutrophil (Ly6G+) dynamics, the initial grid is seeded with resident neutrophils to match the *in vivo* neutrophil distributions of the *Control* group. The objective function for parameter optimization in the neutrophil infiltration simulations consists of the mean and standard

deviation of overall Ly6G + density. The neutrophil density is very high causing a large amount of clustering that is not necessarily due to heterogeneous distribution. This makes the DBSCAN results for this data unreliable [35]. As in the experimental study, neutrophil progression is tracked from *Control* to *Protect* and *Control* to *4xH30*.

The objective function for the progression of neutrophil infiltration is

$$O_F = \frac{1}{N}\sum_{i=1}^{N}\left(\left|\frac{\left(\mu_D^E - \mu_D^S\right)}{\mu_D^E}\right| + \left|\frac{\left(\sigma_D^E - \sigma_D^S\right)}{\sigma_D^E}\right|\right), \quad (5)$$

where all variables have the same meanings as those of Equation 4.

Parameter Optimization

P_{Base} and P_{Local} are identified for each value of r separately. Values of increasing r are tested until the optimized value of the objective function at the current value of r is greater than that of the previous r value (e.g., if the optimization at $r = 3$ *cells* yields a greater objective function value than $r = 2$ *cells*, then $r = 4$ *cells* will not be tested).

For each run of the model, the simulated density is compared to the projected experimental density at every timestep; if *simulated density*$(t_{step}) > 1.5 \times$ *experimental density*(t_{step}) the simulation is terminated. This saves time on computationally expensive parameter sets that generate unreasonably high densities.

Coarse, uniform grid searches are performed for each value of r using larger time steps and a single iteration for each unique set of model parameters. These relatively quick searches allow us to visualize the overall layout of the error surface. These error surface estimations are used to conservatively refine the bounds used for particle swarm optimization (MATLAB *particleswarm* function). The number of particles in the swarm (*SwarmSize*) is set to 50, and the iterations stop when the relative change in the objective function value over the last 20 iterations (*MaxStallIterations*) is less than the specified tolerance of $1\text{x}10^{-3}$ (*FunctionTolerance*). The tolerance is conservatively set based on the standard error present in the stochastic model.

Parameter Bounds for Optimization

The maximum possible P_{Base} for each ventilation pattern is found by setting $P_{Base\ Pre-Normalization}$ in Equation 2 to the mean overall density at the end time in units of # *Injured Cells*/# *Total Cells* (converted from the [31] units of # *Injured Cells*/μm^2 using the density of all cells in the lung). The maximum possible P_{Local} is equal to the total number of cells within the selected region of interdependence (defined by the r value): when $r = 1$ *cell*, $P_{Local} = 6$; when $r = 2$ *cells*, $P_{Local} = 32$; when $r = 3$ *cells*, $P_{Local} = 122$; etc. The lower bounds are set to 0 for both P_{Base} and P_{Local}.

Finding Joint Confidence Intervals

Due to the stochastic nature of the model, the error surfaces contain noise/discontinuities (Fig. 5A, B, Supplemental Videos 1&2) and the optimizer does not find the exact same solution every time. Therefore, the best-fit parameter values are better defined as a region (termed *estimated joint confidence interval*) rather than a single point. To avoid having to run the computationally intensive optimization many times, we perform a fine grid search around the best-fit parameter values to determine these parameter regions of best fit.

Each optimization (e.g., unique ventilation group and unique value of r) is run twice. The bounds for the fine grid search are determined through visual inspection of these error surfaces. A mesh grid containing 400 points (20 evenly spaced P_{Base} values and 20 evenly space P_{Local} values) is then used. The joint confidence interval is the boundary at which the maximum of the optimizers best-fit value (mean + standard error) intersects with the minimum of the surrounding grid points (mean – standard error).

Parameter Interdependence

The interdependence between each set of optimized parameters (P_{Base}, P_{Local}, and r) is determined. These values are calculated by using the error surface (Fig. 5B) and interpolating between the particle swarm optimization points (Fig. 5A). For example, to calculate the interdependence between P_{Local} and P_{Base}, the error surface from the best-fit value of r is used. A set of P_{Base} values are selected and, for each value of P_{Base}, the P_{Local} value yielding the minimum objective function is found. Note that the minimum objective function values are greater than the global minimum. Spearman's correlation coefficients (MATLAB *corr* function with *type* set to '*Spearman*') are then calculated for the set of P_{Base}, P_{Local} coordinates. The correlations are found for each set of parameters; the resulting coefficients are shown in Table 2.

Sensitivity Analysis

Sensitivity analyses are performed for each optimized parameter. P_{Base} and P_{Local} values are individually varied by ± 5% and ± 25% while all other values are kept the same. r values are varied by ± 1 cell while all other values are kept the same.

Table 2 Spearman's correlation coefficients for each set of optimized parameters

	Baseline probability, P_{Base}	Local density probability, P_{Local}	Radius of interdependence, r
Baseline probability, P_{Base}	1	− 0.9434	0.4286
Local density probability, P_{Local}	− 0.9434	1	− 0.4857
Radius of interdependence, r	0.4286	− 0.4857	1

P_{Local} and P_{Base} are strongly correlated. There is a weak interdependence between both P_{Local} and r; and P_{Base} and r

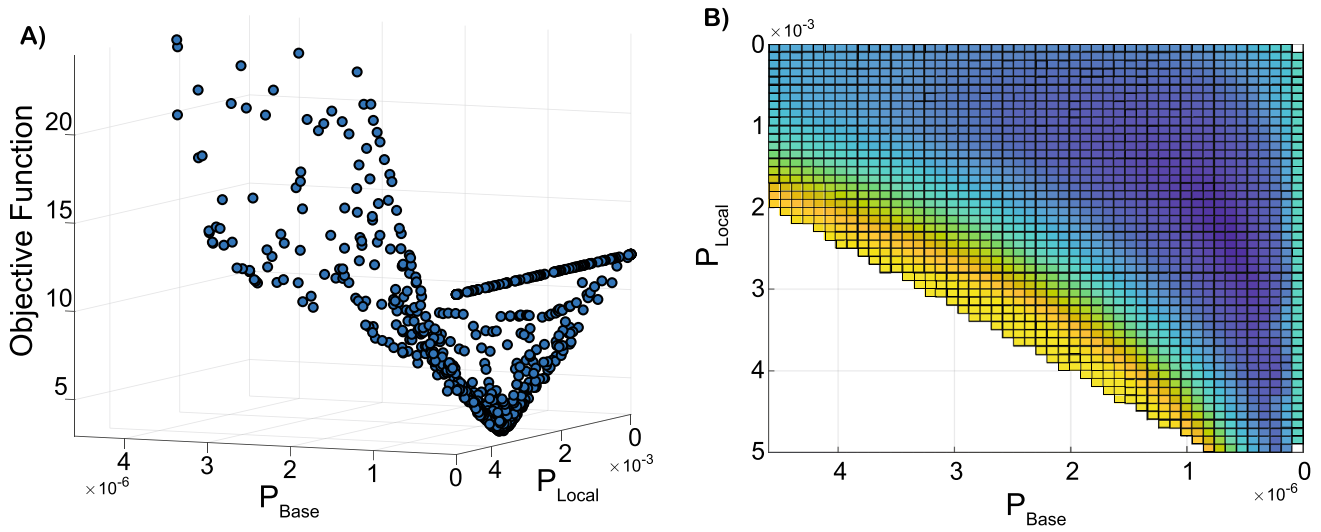

Fig. 5 Representative error (objective function) surface resulting from particle swarm optimization. **A** Data points sampled during particle swarm optimization. **B** 2-Dimensional view of error surface plot found through linear interpolation of sampled particles (parameter sets)

Statistical Analysis

Data are tested for normal distribution using Anderson-Darling tests (significance level = 0.05). The distributions of cellular injury density are not normally distributed for any groups (Fig. 7B). Cluster sizes of cellular injury are normally distributed for *Protect* and *1.1xH30*, but not for the other groups (Fig. 9). The distributions of neutrophil density are normally distributed for all groups (Fig. 10B). All datasets that are non-normally distributed contain sufficiently high sample sizes to qualify for parametric statistical tests [36]. Two-sample *t* tests are used to compare corresponding simulated and experimental data for each group. The normality tests and *t* tests are performed in MATLAB.

Results

Summary of Previous Spatiotemporal Analysis

A robust analysis of the distributions of cellular injury during VILI progression shows that VILI begins as diffuse injury in quasi-random locations. Injury progression is characterized by the expansion of existing regions of injury as well as new, diffuse injury formation. Neutrophil infiltration is shown to follow a more systemic response during ventilation, which is not dependent on ventilation pattern [31]. These findings inform the formulation of the computational model.

Static Parameter Determination

Static parameters are defined to give stable results when the model output produced from that value falls within 5% of the 5 most computationally expensive values tested. The minimum grid size that provides stable model results is found to be 130 cells in cubic length (Fig. 4A) for a total of 2,197,000 cells in the domain. The minimum number of iterations (repeated runs with the same parameters) required for a stable fit is 40 (Fig. 4B). Since the computer cluster used to run the simulations contains 64 cores per node, we used 64 iterations to maximize resource utilization.

The model output does not converge until the timestep $\lesssim$ 2.5 seconds (> 2719 time steps for *p37.5*) as shown in Fig. 4C&D. Optimization run times were excessive with

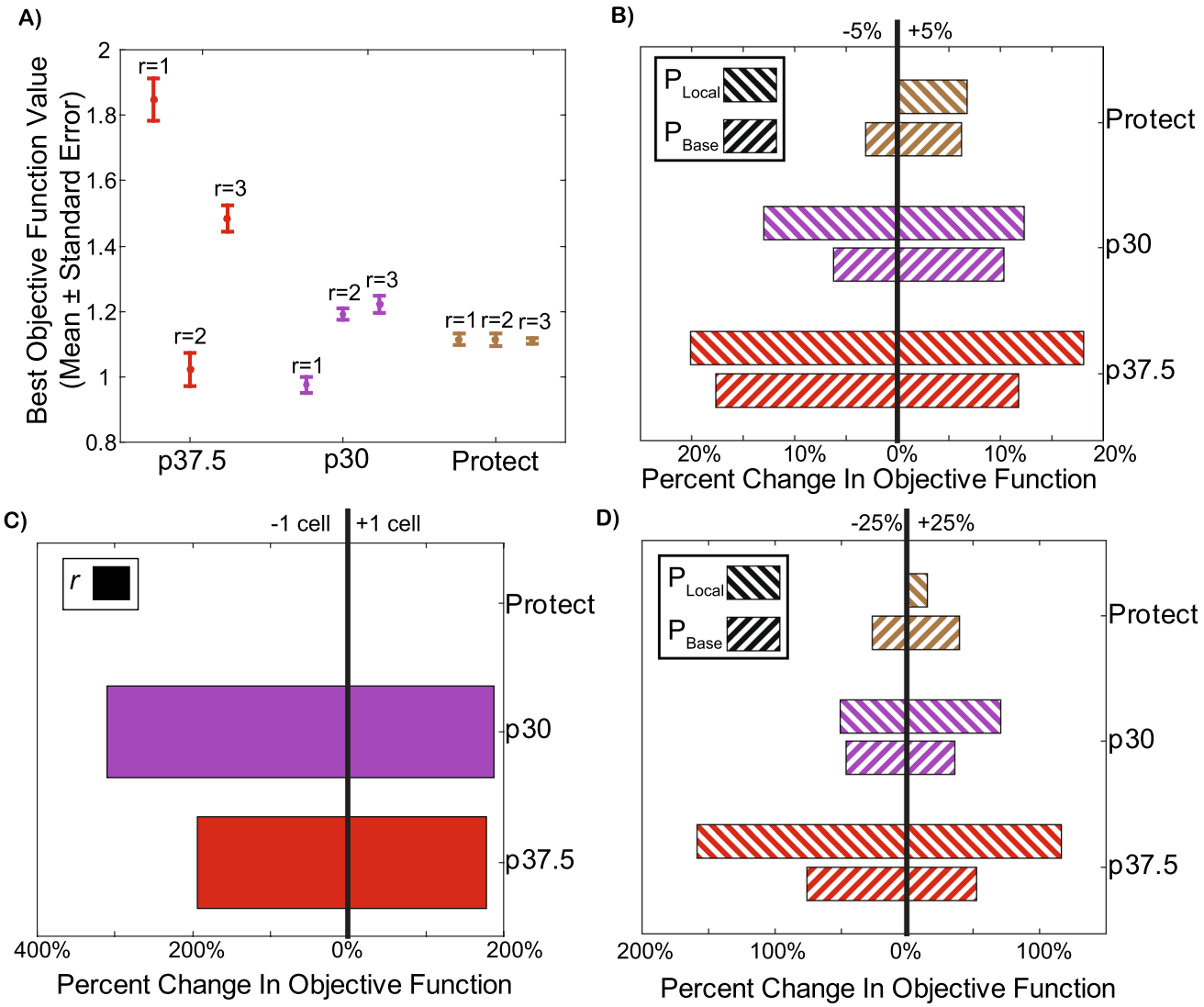

Fig. 6 **A** Mean (points) and standard error (bars) of the cellular injury best-fit objective functions at different values of r. *p37.5* is significantly better at $r = 2$ *cells* than at any other r value. The best fit for *p30* is found at $r = 1$ *cell*. *Protect* has no significant differences across r values because the best fit is at $P_{Local} = 0$. **B** Sensitivity analysis of 5% change in P_{Local} and P_{Base} for cellular injury. *Protect* P_{Local} is tested at zero (no bar), the best-fit value, and 2×10^{-7}, a value slightly outside the *Protect* joint confidence interval. **C** Sensitivity analysis of 1 cell change in r for cellular injury. *Protect* is not affected by changes to r because the best-fit value of P_{Local} is zero. **D** Sensitivity analysis of 25% change in P_{Local} and P_{Base} for cellular injury. *Protect* P_{Local} is tested at zero (no bar), the best-fit value, and 2×10^{-5}

such a small timestep; therefore, we chose a timestep of 12 seconds where the curve visually starts to plateau (Fig. 4C). Although we could not optimize the model at the ideal timestep, the developed timestep-dependent equations (Equations 2&3) do eventually plateau as is evident in the log–log plot (Fig. 4D).

Parameter Interdependence

Analysis of parameter interdependence (Table 2) reveals a strong inverse relationship between P_{Base} and P_{Local}, where an increase in P_{Base} causes a consistent decrease in P_{Local}. P_{Base} and r have a weak positive correlation. P_{Local} and r have a weak inverse correlation.

Cellular Injury Simulations

Figure 6A shows that the minimum objective function (the best fit) is found when $r = 2$ *cells* for *p37.5* and $r = 1$ *cell* for *p30* ventilation. The *Protect* group has a minimum objective function at $P_{Local} = 0$ so the value of r is irrelevant (Equation 1). Accordingly, all the analyses of the *Protect* group are done at $r = 1$ *cell*. The injurious ventilation groups (*p30*

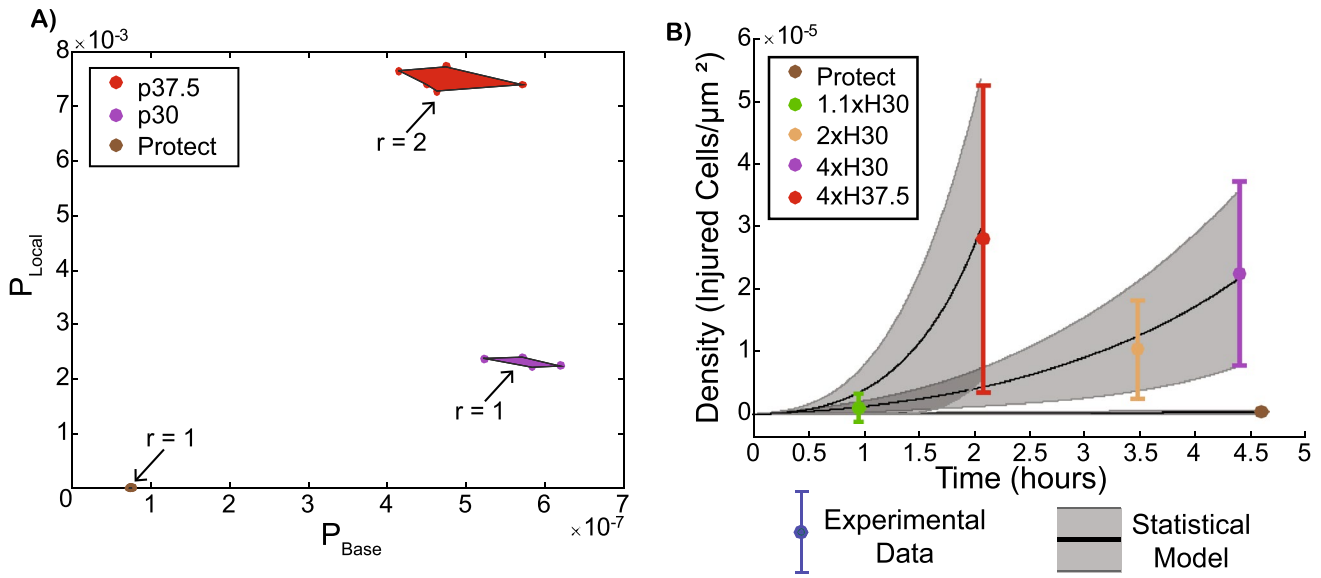

Fig. 7 **A** Joint confidence intervals for cellular injury optimizations. *p37.5* confidence interval (red region) is shown for $r = 2$ *cells*; *p30* (purple region) and *Protect* (brown region) confidence intervals are shown for $r = 1$ *cell*. **B** Mean (colored dots) and standard deviation (colored error bars) of experimental injury density are compared to mean (black line) and standard deviation (gray-shaded region) of simulated injury progression. No statistical differences are found between the experimental data and the corresponding simulated injury densities

and *p37.5*) have significantly better solutions at the best-fit values of *r*.

Joint confidence intervals for the best-fit parameters for each group's respective values of *r* are shown in Fig. 7A and the parameter values are listed in Table 3. Both injurious ventilation patterns (*p30* and *p37.5*) show significant elevation of P_{Base} over *Protect*. P_{Local} shows significant increases with ventilation harmfulness (*Protect* → *p30* → *p37.5*); *r* also increases with ventilation severity.

Cellular injury density correlates well between the experimental and simulated data (Fig. 7B) with no significant differences between corresponding groups. The means of the experimental densities and their corresponding simulated densities show no significant differences (Fig. 7B). The full distributions of cellular injury (Fig. 8) also show qualitative correlation with their simulated counterparts: all groups show a right skewness and similar values of outlier data points. Both Figs. 7B and 8 use each tissue slice as a data point.

Cellular injury cluster size also correlates well between the experimental and simulated data (Fig. 9A). No corresponding groups show significant differences between experimental and simulated data at a significance value of $p < 0.05$. The full distributions of cluster size (Fig. 9B) show qualitative correlation as well, having similar skewness and outliers.

Sensitivity analysis of P_{Base} and P_{Local} (Fig. 6B) show that a 5% change in parameter values cause a greater percentage change in the objective function for the injuriously ventilated groups (*p30* and *p37.5*). *Protect* shows a dampened response to changes in P_{Base}, which is not unexpected as this group contains very minimal injury. *Protect* P_{Local} is tested at zero (the best-fit value) and 2×10^{-7} (a value slightly outside the *Protect* joint confidence interval). A 25% change in parameter values P_{Base} and P_{Local} causes a

Table 3 Best-fit parameter values for all groups

Marker	Cellular injury			Neutrophils	
Experimental group	*Protect*	*p30*	*p37.5*	*Protect*	*p30*
Baseline probability, $P_{Base}(\times 10^{-7})$	0.77	5.9	4.7	160	1.3
Local density probability, $P_{Local}(\times 10^{-3})$	0	2.4	7.4	1.2	3.1
Radius of interdependence, r	N/A	1 cell or 33 μm	2 cells or 66 μm	5 cells or 165 μm	8 cells or 264 μm

Radius of interdependence is shown in units of grid cells and micrometers (converted using the grid spacing). The micrometer spacing is used to compare model results to previous studies

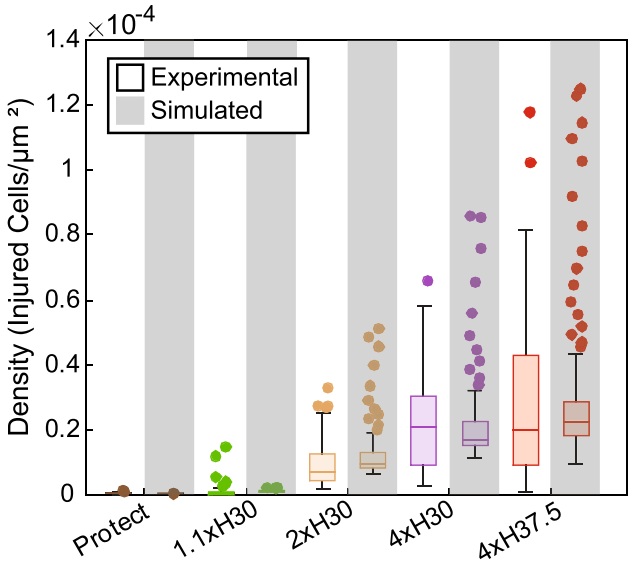

Fig. 8 Comparisons of cellular injury density distributions (box plots) between the experimental data (white background) and simulated data (gray background) for all ventilation groups

greater than 25% change in the resulting objective function (Fig. 6D). Here, the changed value of *Protect* P_{Local} is set to 2×10^{-5}. A 1 cell change in r causes a greater than 100% change in the resulting objective function (Fig. 6C). Changes in r do not alter the objective function for *Protect* as the best-fit value of $P_{Local} = 0$ (the r value is obsolete).

Neutrophil Infiltration Simulations

In the neutrophil infiltration simulations, the objective function is minimized at $r = 8$ *cells* for *p30* and $r = 5$ *cells* for *Protect* (Fig. 10A). The joint confidence intervals of best fit for these r values are shown in Fig. 10A, and the best-fit parameter values are in Table 3. *Protect* has a significantly higher P_{Base}, while *p30* has a significantly greater P_{Local}. The simulated progression of neutrophil infiltration correlates with the experimental data (Fig. 10B).

The minimum objective function (best fit) for the neutrophil simulations is found when $r = 5$ *cells* for *Protect* and $r = 8$ *cells* for *p30* ventilation. Both groups have significantly better solutions at the best-fit values of r (Fig. 11A). Sensitivity analyses show that a 5% change in parameter values P_{Base} and P_{Local} causes a greater than 5% change in the resulting objective function (Fig. 11B); a 25% change in parameter values P_{Base} and P_{Local} causes a greater than 25% change in the resulting objective function (Fig. 11D); and a 1 cell change in r causes a greater than 10% change in the resulting objective function (Fig. 11C).

Discussion

Our prior quantitative analyses of cellular injury and neutrophil distributions during VILI [31] revealed that VILI progression is characterized by initiation of diffuse damage (cellular injury formation and neutrophil accumulation) in

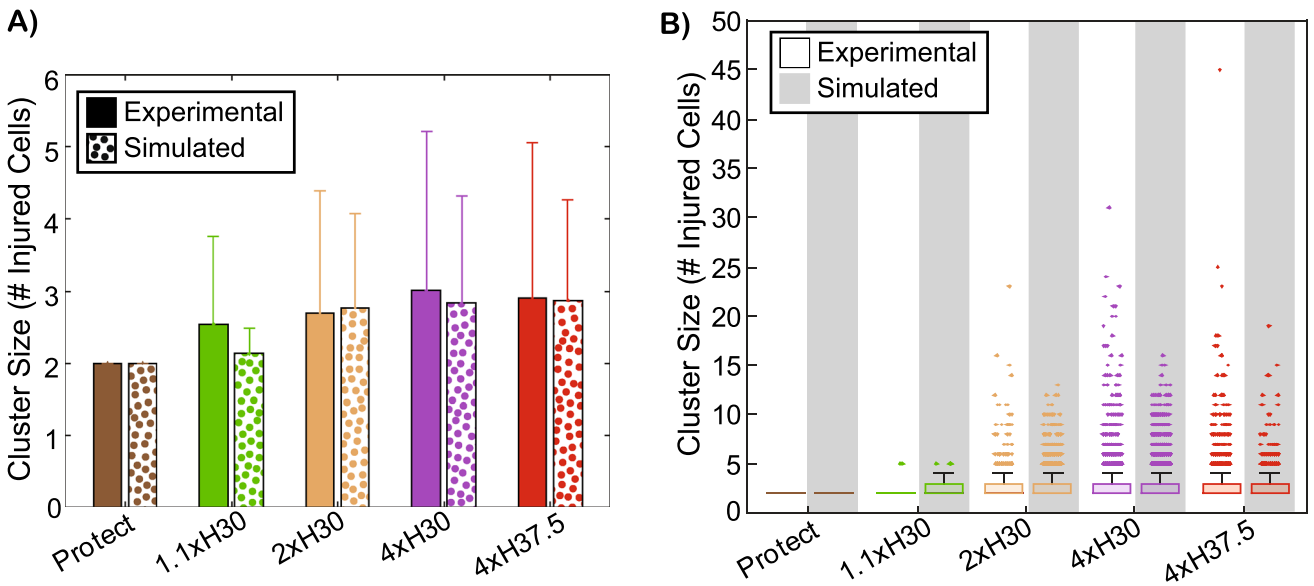

Fig. 9 **A** Comparisons of mean and standard deviation of cellular injury cluster size. Statistical comparisons are performed between corresponding experimental (solid bars) and simulated (dotted bars) data. No ventilation groups show significant differences between simulated data (dotted bars) and corresponding experimental data (solid bars) at $p<0.05$. **B** Comparisons of cellular injury cluster size distributions (box plots) between the experimental data (white background) and simulated data (gray background) for all ventilation groups

quasi-random locations and the expansion of existing damaged regions. To further understand that rich experimental dataset, we developed a cellular automata-based computational model governed by the baseline probability of damage occurring (P_{Base}), the strength of interdependence between existing and new damaged regions (P_{Local}), and the range of interdependence between these damaged regions (r). The stochastic model successfully fits datasets that start with no positively marked cells (PI+, cellular injury) and datasets that start with a resident population of positively marked cells (Ly6G+, neutrophils). The optimized parameter values provide simple, direct comparisons between groups which are easy to interpret and provide insight into system dynamics of VILI progression. Sensitivity analyses reveal that all three optimized parameters are important to the model dynamics.

During cellular injury progression, the probability of randomly located injury (P_{Base}) increases with injurious compared to protective ventilation. The range (r) and strength (P_{Local}) of interdependence between existing and new injury also increases as ventilation pressure increases (Fig. 7A; Table 3). This interdependence between injured regions plays the dominant role in VILI progression, which relates to the high levels of heterogeneity (Fig. 7B, red and purple error bars; Fig. 8) and injury clustering (Fig. 9A, B) observed in these groups experimentally [31]. We postulate that mechanical tethering forces are the driver behind this interdependence because the best-fit radii for the injuriously ventilated groups (Table 3, r) correlate with those found in finite element models of strain propagation – greatest strain increases extend ~ 2 alveolar diameters (≈100 μm for our study) out from a central stiffened 'alveolus' [37]. Our observed increase in r as ventilation pressure increases (*Protect* → *p30* → *p37.5*) also correlates with finite element models: increasing the induced strain [37] and increasing the size of an existing region of damage [38] causes increases in the range of strain propagation.

Interdependence also affects infiltrating neutrophils, with injurious ventilation (*p30*) being more heavily influenced by interdependence compared to protective ventilation (*Protect*) (Fig. 10A). This correlates with previous cellular automata models of the targeted response of immune cells to localized areas of injury [39] and high strain regions [40]. Our prior quantification of neutrophil distributions did not suggest heterogeneous distributions or differences between *p30* and *Protect* ventilation [31]; the model optimization reveals novel insights not available from data analysis alone. The radii of interdependence for these groups are much higher than that of cellular injury (Table 3). These ranges of interdependence are not readily explainable by tethering forces or atelectrauma, and are likely due to longer-range signaling mechanisms [41].

Limitations

This model is a relatively simple, computationally tenable simulation of a very complicated problem. Increasing the model complexity dramatically increased the computation time, so the current version was used as a first pass at defining the dynamics of VILI propagation. In the future, more

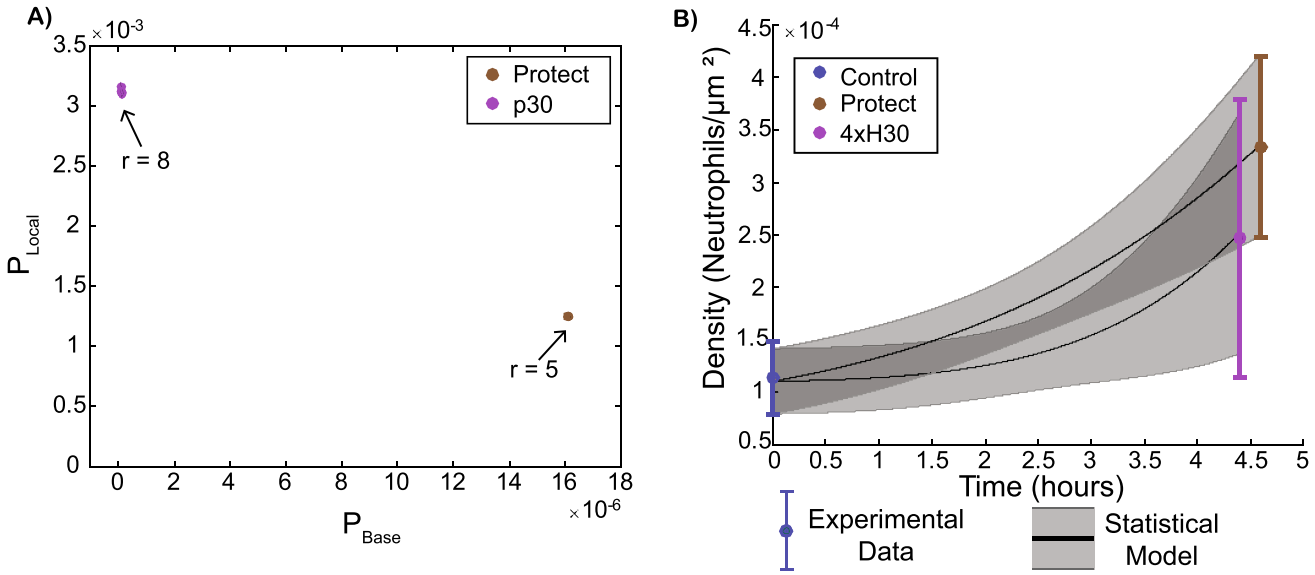

Fig. 10 **A** Joint confidence intervals for neutrophil infiltration parameters. *p30* confidence interval (purple region) is shown for $r = 8$ *cells*; *Protect* confidence interval is shown for $r = 5$ *cells*. **B** Mean (colored dots) and standard deviation (colored error bars) of experimental neutrophil density are compared to mean (black line) and standard deviation (gray-shaded region) of simulated neutrophil infiltration. No statistical differences are found between the experimental data and the corresponding simulated neutrophil densities

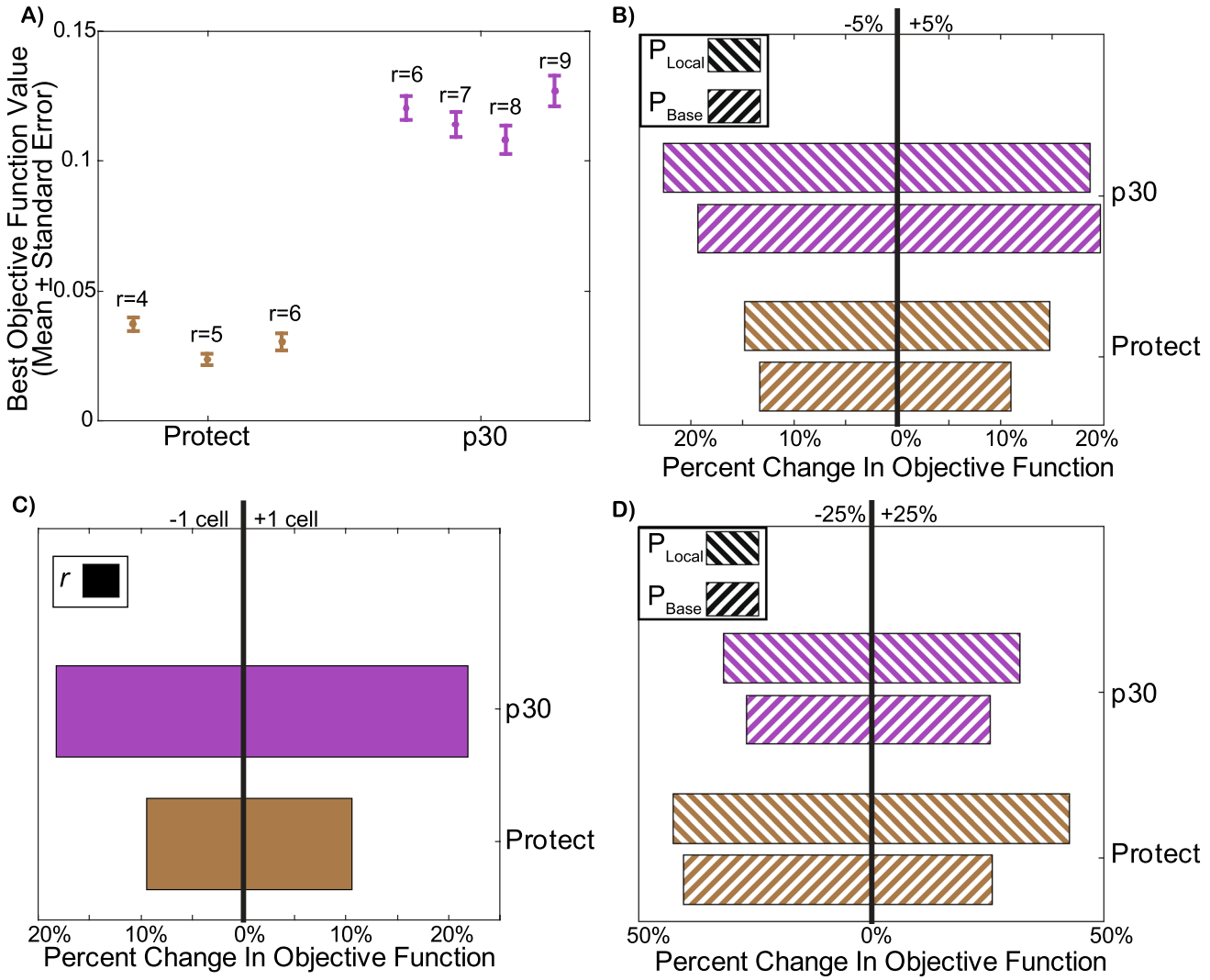

Fig. 11 **A** Mean and standard error of the neutrophil infiltration best-fit objective functions at different r values. *Protect* is significantly better at $r = 5$ *cells* than at any other r value. The best fit for *p30* is found at $r = 8$ *cells*; this is significantly better than all other r values except $r = 7$ (there is overlap in the standard error for $r = 7$ and $r = 8$ best fits). **B** Sensitivity analysis of 5% change in P_{Local} and P_{Base} for infiltrating neutrophils. **C** Sensitivity analysis of 1 cell change in r for infiltrating neutrophils. **D** Sensitivity analysis of 25% change in P_{Local} and P_{Base} for infiltrating neutrophils

complex versions of the model (e.g., a dynamic region of influence) could be implemented to better replicate the experimental data. For reference, a single iteration of the deployed model for the best-fit parameters of *p30* takes ~ 15 minutes to run on two AMD EPYC 7502 32 core processors with 512 GB of DDR4 memory. The run time of a single iteration varies greatly depending on the parameter values and the simulated ventilation time (increases in P_{Base}, P_{Local}, r, or ventilation time all increase run time). Particle swarm optimization within refined bounds (as detailed in the Materials and Methods—Parameter Optimization section) takes between 3–7 days to converge.

The limited experimental data used to fit the model also introduce limitations. The *p30* PI + data are fit to 4 time points and all other progressions are only fit to 2 time-points. While parameter optimization shows that a single region of unique best-fit values exists for each experimental group (Fig. 5A, B and Supplemental Videos 1&2), adding additional data points could alter these best-fit parameters and facilitate more complete physiological interpretations. Future studies can increase the number of experimental timepoints sampled for each ventilation pattern.

The experimental data used for parameter optimization are that of pure VILI with no pre-existing injury.

Mechanical ventilation has been shown to induce lung injury even in initially healthy lungs. However, future studies may perform this entire study on a model of pre-existing lung injury, which would provide more relevant physiological insights into ventilation of predisposed lungs (e.g., ARDS patients). These studies could be performed with the existing model, as illustrated by the successful recapitulation of neutrophil progression which begins with resident populations of damaging cells.

Also note that the model was designed to recapitulate the behavior of cellular injury (PI +) progression. The neutrophil infiltration is fit using the same model for comparative purposes, but there are some added limitations in this application. Namely, there are a set number of cells available in this model with pre-defined locations, based on total cell density in the lung. *In vivo,* more cells could be added to the lung/grid as neutrophils infiltrate.

Summary

To summarize, our novel stochastic model recapitulates VILI progression in two markers of damage—cellular injury and infiltrating neutrophils—during both lung-protective and injurious ventilations. Model parameter optimization using experimental data simplifies and explains the findings of complex quantitative analyses and provides additional insights that are not apparent from data analysis alone. The range and strength of interdependence between damaged regions are shown to increase as ventilation patterns become more harmful. In the future, these methods could be applied to different ventilation patterns, injury models, or organ systems to determine which conditions minimize detrimental interdependency.

Supplementary Information The online version contains supplementary material available at https://doi.org/10.1007/s10439-023-03346-3.

Acknowledgements This work was supported by the National Institutes of Health Grants R01 HL151630 ("Predicting and Preventing Ventilator-Induced Lung Injury"; to B.J.S.) and F31 HL149268 ("Spatiotemporal evolution of lung injury during ventilator-induced lung injury"; to C.L.M.); and National Science Foundation Grant 2225554 ("'RECODE: Defining Environmental Design Criteria for Directed Differentiation of Type 1 from Type 2 Lung Alveolar Epithelial Cells," to B.J.S and C.L.M.). This work used the computing resources at the Center for Computational Mathematics, University of Colorado Denver, including the Alderaan cluster, supported by the National Science Foundation award OAC-2019089.

Declarations

Conflict of interest The authors have no conflicts of interest to disclose.

References

1. Ware, L. B., and M. A. Matthay. The acute respiratory distress syndrome. *N. Engl. J. Med.* 342(18):1334–1349, 2000.
2. Force, A. D. T., et al. Acute respiratory distress syndrome: the Berlin Definition. *JAMA*. 307(23):2526–2533, 2012.
3. Andrade, M. C., et al. Applying positive end-expiratory pressure during mechanical ventilation causes pulmonary redox imbalance and inflammation in rats. *Shock*. 50(5):572–578, 2018.
4. Choudhury, S., et al. Mechanisms of early pulmonary neutrophil sequestration in ventilator-induced lung injury in mice. *Am. J. Physiol. Lung. Cell Mol. Physiol.* 287(5):L902–L910, 2004.
5. Seah, A. S., et al. Quantifying the roles of tidal volume and PEEP in the pathogenesis of ventilator-induced lung injury. *Ann. Biomed. Eng.* 39(5):1505–1516, 2011.
6. Slutsky, A. S. Lung injury caused by mechanical ventilation. *Chest*. 116(Suppl. 1):9S-15S, 1999.
7. Slutsky, A. S., and Y. Imai. Ventilator-induced lung injury, cytokines, PEEP, and mortality: implications for practice and for clinical trials. *Intens. Care Med.* 29(8):1218–1221, 2003.
8. Taskar, V., et al. Surfactant dysfunction makes lungs vulnerable to repetitive collapse and reexpansion. *Am. J. Respir. Crit. Care Med.* 155:313–320, 1997.
9. Villar, J., et al. The ALIEN study: incidence and outcome of acute respiratory distress syndrome in the era of lung protective ventilation. *Intens. Care Med.* 37(12):1932–1941, 2011.
10. Kaczka, D. W., et al. Quantifying mechanical heterogeneity in canine acute lung injury: impact of mean airway pressure. *Anesthesiology*. 103(2):306–317, 2005.
11. Sinclair, S. E., N. L. Polissar, and W. A. Altemeier. Spatial distribution of sequential ventilation during mechanical ventilation of the uninjured lung: an argument for cyclical airway collapse and expansion. *BMC Pulm. Med.* 10:25, 2010.
12. Fagerberg, A., et al. Electrical impedence tomography and heterogeneity of pulmonary perfusion and ventilation in porcine acute lung injury. *Acta Anaesthesiol. Scand.* 53(10):1300–1309, 2009.
13. Porra, L., et al. Quantitative imaging of regional aerosol deposition, lung ventilation and morphology by synchrotron radiation CT. *Sci. Rep.* 8(1):3519, 2018.
14. Stahr, C. S., et al. Quantification of heterogeneity in lung disease with image-based pulmonary function testing. *Sci. Rep.* 6:29438, 2016.
15. Gattinoni, L., and A. Pesenti. The concept of "baby lung." *Intens. Care Med.* 31(6):776–784, 2005.
16. Perlman, C. E., D. J. Lederer, and J. Bhattacharya. Micromechanics of alveolar edema. *Am. J. Respir. Cell Mol. Biol.* 44(1):34–39, 2011.
17. Costa, E. L., et al. Mild endotoxemia during mechanical ventilation produces spatially heterogeneous pulmonary neutrophilic inflammation in sheep. *Anesthesiology*. 112(3):658–669, 2010.
18. Gajic, O., et al. Ventilator-induced cell wounding and repair in the intact lung. *Am. J. Respir. Crit Care Med.* 167(8):1057–1063, 2003.
19. Le, A., et al. Alveolar cell apoptosis is dependent on p38 MAP kinase-mediated activation of xanthine oxidoreductase in ventilator-induced lung injury. *J. Appl. Physiol.* 105(4):1282–1290, 2008.
20. Makena, P. S., et al. Deletion of apoptosis signal-regulating kinase-1 prevents ventilator-induced lung injury in mice. *Am. J. Respir. Cell Mol. Biol.* 46(4):461–469, 2012.
21. Otto, C.M., et al., *Spatial and temporal heterogeneity of ventilator-associated lung injury after surfactant depletion.* J. Appl. Physiol. (1985), 2008. **104**(5): p. 1485-94.
22. Sinclair, S. E., et al. Positive end-expiratory pressure alters the severity and spatial heterogeneity of ventilator-induced lung

injury: an argument for cyclical airway collapse. *J. Crit. Care*. 24(2):206–211, 2009.
23. Wellman, T. J., et al. Effect of local tidal lung strain on inflammation in normal and lipopolysaccharide-exposed sheep. *Crit. Care Med.* 42(7):e491-500, 2014.
24. Motta-Ribeiro, G., et al., *Spatial Heterogeneity of Lung Strain and Aeration and Regional Inflammation During Early Lung Injury Assessed with PET/CT.* Acad Radiol, 2018.
25. Paula, L. F., T. J. Wellman, T. Winkler, P. M. Spieth, A. Güldner, J. G. Venegas, M. Gama de Abreu, A. R. Carvalho, and M. F. Vidal Melo. Regional tidal lung strain in mechanically ventilated normal lungs. *J. Appl. Physiol.* 121(6):1335–47, 2016.
26. Yen, S., et al., *The Link between Regional Tidal Stretch and Lung Injury during Mechanical Ventilation.* Am. J. Respir. Cell Mol. Biol. **0**(ja): p. null.
27. Ma, B. and J.H. Bates, *Continuum vs. spring network models of airway-parenchymal interdependence.* J. Appl. Physiol. (1985), 2012. **113**(1): p. 124-9.
28. Ma, B., B. Breen, and J. H. Bates. Influence of parenchymal heterogeneity on airway-parenchymal interdependence. *Respir. Physiol. Neurobiol.* 188(2):94–101, 2013.
29. Ma, B., B. J. Smith, and J. H. Bates. Resistance to alveolar shape change limits range of force propagation in lung parenchyma. *Respir. Physiol. Neurobiol.* 211:22–28, 2015.
30. Ma, B. S., and J. H. T. Bates. Mechanical interactions between adjacent airways in the lung. *J. Appl. Physiol.* 116(6):628–634, 2014.
31. Mattson, C.L., et al., Spatiotemporal distribution of cellular injury and leukocytes during the progression of ventilator-induced lung injury. *Am. J. Physiol. Lung Cell. Mol. Physiol.* 2022; 323(3):281–96
32. Tsuno, K., et al. Histopathologic pulmonary changes from mechanical ventilation at high peak airway pressures. *Am. Rev. Respir. Dis.* 143(5):1115–1120, 1991.
33. Villar, J., et al. Experimental ventilator-induced lung injury: exacerbation by positive end-expiratory pressure. *Anesthesiology*. 110(6):1341–1347, 2009.
34. Hirsch, J., et al. Double impact of cigarette smoke and mechanical ventilation on the alveolar epithelial type II cell. *Crit. Care*. 18(2):R50, 2014.
35. Mattson, C., et al., *Spatiotemporal Distribution of Cellular Injury and Leukocytes during the Progression of Ventilator-Induced Lung Injury: Online Supplement*. 2022: figshare.
36. Blanca, M. J., et al. Non-normal data: is ANOVA still a valid option? *Psicothema*. 29(4):552–557, 2017.
37. Makiyama, A. M., et al. Stress concentration around an atelectatic region: a finite element model. *Respir. Physiol. Neurobiol.* 201:101–110, 2014.
38. Albert, R. K., et al. Is progression of pulmonary fibrosis due to ventilation-induced lung injury? *Am. J. Respir. Crit. Care Med.* 200(2):140–151, 2019.
39. Reynolds, A., et al. Cellular automata modeling of pulmonary inflammation. *Mol. Cell Biomech.* 9(2):141–156, 2012.
40. Ibrahim, I. B. M., O. V. S. Sarma, and R. M. Pidaparti. Simulation of healing threshold in strain-induced inflammation through a discrete informatics model. *IEEE J. Biomed. Health Inform.* 22(3):935–941, 2018.
41. Wilson, M. R., and M. Takata. Inflammatory mechanisms of ventilator-induced lung injury: a time to stop and think? *Anaesthesia*. 68(2):175–178, 2013.